Strong-coupling anisotropic *s*-wave superconductivity in the type-II Weyl semimetal $TaIrTe_4$

Diandong Tang,[1,2,*] Yan Chen,[3,4,5,*] Meng Yang,[6,7,*] Qiming Wang,[8] Yuxiao Zou,[3,4] Xin Wang,[1] Zezhong Li,[1] Changjiang Yi,[6] Youguo Shi,[4,6] Xiangmu Kong,[8,9] Guofeng Song,[3,4] Yun Xu,[3,4,5] Xin Wei,[3,4] Michael Weinert,[2] Lian Li,[10,†] Weihai Fang,[1,‡] and Ying Liu[1,§]

[1]*College of Chemistry, Beijing Normal University, Beijing 100875, China*
[2]*Department of Physics, University of Wisconsin-Milwaukee, Milwaukee, Wisconsin 53201, USA*
[3]*Institute of Semiconductors, Chinese Academy of Sciences, Beijing 100083, China*
[4]*Center of Materials Science and Optoelectronics Engineering, University of Chinese Academy of Sciences, Beijing 100049, China*
[5]*Beijing Key Laboratory of Inorganic Stretchable and Flexible Information Technology, Beijing 100083, China*
[6]*Beijing National Laboratory for Condensed Matter Physics and Institute of Physics, Chinese Academy of Sciences, Beijing 100190, China*
[7]*School of Physical Sciences, University of Chinese Academy of Sciences, Beijing 100049, China*
[8]*College of Physics and Engineering, Qufu Normal University School, Qufu 273165, China*
[9]*School of Physics and Optoelectronic Engineering, Ludong University, Yantai 264025, China*
[10]*Department of Physics and Astronomy, West Virginia University, Morgantown, West Virginia 26506, USA*

(Received 15 October 2020; accepted 19 April 2021; published 17 May 2021)

$TaIrTe_4$ is a recently discovered type-II Weyl semimetal, hosting only four Weyl points. Here, we study the cleaved $TaIrTe_4$ crystal using scanning tunneling microscopy/spectroscopy and find that it also hosts a superconducting state with a transition temperature of 3.9 K. From Dynes function fitting, the superconducting phase is consistent with anisotropic *s*-wave pairing, with a superconducting gap of 1.31 meV. This value leads to a value of $2\Delta_{\max}/k_BT_C = 7.81$, much larger than the 3.53 predicted by Bardeen-Cooper-Schrieffer theory for weak-coupling superconductors. The critical field is found to be 0.7 T based on the analysis of tunneling conductance as a function of magnetic field. Two types of nonmagnetic defects on the $TaIrTe_4$ surface are observed, neither of which induce bound states inside the superconducting gap, further supporting conventional *s*-wave superconductivity in the $TaIrTe_4$ system.

DOI: 10.1103/PhysRevB.103.174508

Type-II Weyl semimetals, exhibiting Weyl cones at the crossings of electron and hole pockets [1–3], have attracted much attention recently as a quantum phase of matter [1–9], which violates Lorentz invariance, leading to tilted Weyl cones and Weyl points with finite density of states. In addition to properties similar to type-I Weyl semimetals, such as topologically protected surface Fermi arcs, chiral anomalies, and large unsaturated magnetoresistances [3,7,9], type-II Weyl semimetal has been predicted to exhibit additional exotic quantum properties, e.g., Landau level collapse [10]. The integration of superconducting and type-II Weyl semimetal phases would provide a new platform for exploring topological superconductivity for quantum information processing. Therefore, searching for superconducting phases in type-II Weyl semimetals is of great interest.

Theoretically, doped Weyl semimetals have been predicted to be topologically unconventional sign changing $s_\pm$ superconductors, hosting robust Majorana fermion surface states [11]. In the type-II Weyl semimetals $MoTe_2$ and WTe_2, superconducting phases are observed under high pressure [12–15], accompanying a structural phase transition [16], with chemical potential tuning by gating [17,18] or doping [19–23]. However, clear evidence is still necessary to support the nontrivial topological nature of the superconducting phase in these two compounds.

$TaIrTe_4$ is the third predicted type-II Weyl semimetal, hosting only four Weyl points, the minimum allowed numbers of Weyl points in a time-reversal symmetry invariant system [5,24]. Time-resolved angle-resolved photoemission spectroscopy showed evidence of Fermi arcs at 100 meV above the Fermi level [25]. Superconductivity has been studied in $TaIrTe_4$ [26,27], and the superconducting symmetry has been suggested to be *p*-wave pairing [26], which indicates a potential topological superconducting state in $TaIrTe_4$. Here, we also observe a superconducting phase in $TaIrTe_4$ using scanning tunneling microscopy (STM)/ scanning tunneling spectroscopy (STS), but the pairing symmetry is found to be consistent with anisotropic *s*-wave from a Dynes function analysis. This identification is further supported by the observation that no in-gap resonant states are induced by nonmagnetic impurities.

As a ternary compound, $TaIrTe_4$ has two typical structural phases, the monoclinic $1T'$ and the orthorhombic T_d phases [28]. The orthorhombic structure has two possible space groups, the centrosymmetric *Pnmm* and the noncentrosymmetric $Pnm2_1$. The T_d $Pnm2_1$ phase has a topologically protected band structure and is categorized as a type-II Weyl semimetal, hosting four separated Weyl points.

*These authors contributed equally to this paper.
†lian.li@mail.wvu.edu
‡fangwh@bnu.edu.cn
§11112017013@bnu.edu.cn

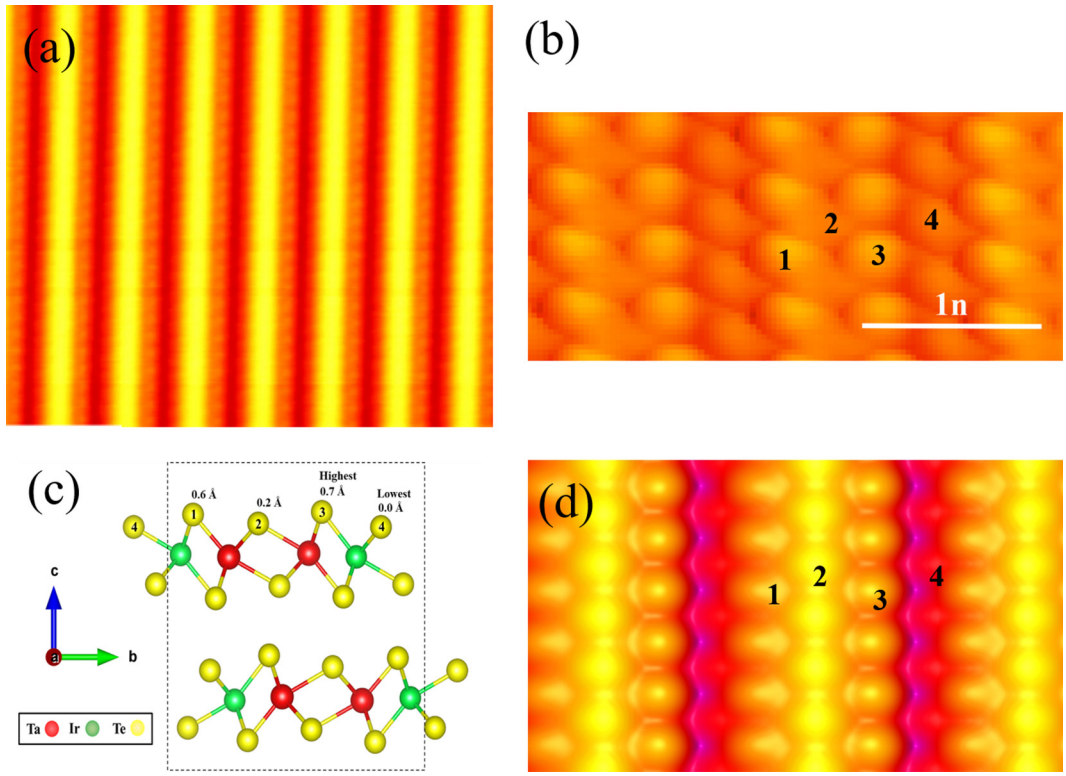

FIG. 1. (a) Scanning tunneling microscopy (STM) image taken on top of the sample, showing the morphology of the cleaved (001) surface (9×9 nm, $V_s = -500$ mV, $I_t = 500$ pA), with chains along the a direction. (b) High-resolution STM image (1.4×3.0 nm, $V_s = -500$ mV, $I_t = 100$ pA). (c) Ball-and-stick model of the optimized $TaIrTe_4$ crystal. Top-layer Te atoms have four sites with slightly different heights, with the relative height of each site given. The dotted square encloses a unit cell. (d) Simulated STM image ($V_{\text{bias}} = -500$ mV) with Te sites labeled as in (c), which lead to the labeling in (b).

The samples studied in this paper were synthesized by the Te-flux technique and confirmed to be T_d phase with space group $Pmn2_1$ by x-ray diffraction (Supplemental Material Figs. S1 and S2 [29]). The T_d phase $TaIrTe_4$ crystals have a layered structure along the c axis. The $TaIrTe_4$ was cleaved along the c axis at 77 K in an ultra-high vacuum chamber with a base pressure of 5×10^{-10} torr. After cleavage, the sample was transferred *in situ* into the STM sample stage to avoid the adsorption of impurities. To obtain high-quality tunneling spectra, we pretreated the STM tips (W and Pt/Ir) on both freshly grown Ag films and Pb samples beforehand to ensure that the surface states of Ag and superconducting gap of Pb were as expected (Supplemental Material Fig. S3 [29]) Under these tip conditions, the tunneling spectra obtained on $TaIrTe_4$ were typically symmetric. To eliminate errors in temperature measurements, we further verified that the superconducting transition temperature of a Pb sample is consistent with earlier reports [30]. The density functional theory (DFT) calculations were performed with the VASP package [31,32], using the Perdew-Burke-Ernzerhof (PBE) functional [33] and an $18 \times 6 \times 1$ Γ-centered K-point mesh.

The STM image in Fig. 1(a) depicts the surface morphology of the cleaved (001) surface. Periodic straight stripelike modulations in the a direction form a bright-dark alternating structure with a spacing $\sim$1 nm. A high-resolution image, Fig. 1(b), demonstrates that the periodic modulation reflects the crystal structure, Fig. 1(c), in which the planes of Ta and Ir atoms are covalently bonded to Te atoms both above and below in each $TaIrTe_4$ layer. To illustrate the origin of the contrast stripes, DFT calculations for the (001) surface were performed using a slab model with four layers of $TaIrTe_4$ and a 15-Å vacuum layer.

Figure 1(c) shows a side view of optimized ball-and-stick model of $TaIrTe_4$ crystal. The Te atoms at the surface have different heights and electronic states. Comparison of the simulated STM image, Fig. 1(d), with the experimental one leads to the identification of the dark trenches as Te atoms between the Ir atoms, while bright ridges are Te atoms between Ta atoms. The corresponding positions of the Te atoms in the STM images are marked in Figs. 1(b) and 1(d), following the notation in the ball-and-stick model, Fig. 1(c).

To probe the superconducting state of the $TaIrTe_4$ (001) surface, STS spectra were obtained, Fig. 2(a), starting from 0.3 K, the minimum available temperature of our instrument. The differential conductance shows a V-shaped gap, reaching minimum value at zero bias. Away from the Fermi energy, two symmetric coherent peaks are well resolved at the energy around ± 1.31 mV, leading to an energy gap with 1.31 meV.

With increasing temperature, the spectra still exhibit the line shape indicative of the superconducting state until 3.9 K, beyond which the superconducting gap totally disappeared, indicating the suppression of the superconducting state. Based on these observations, we conclude the critical temperature T_c of $TaIrTe_4$ is $\sim$3.9 K. Note that a lower T_c of 2.5 K was also observed on a different sample (Supplemental Material Fig. S4 [29]). The T_c of $TaIrTe_4$ is higher than the other

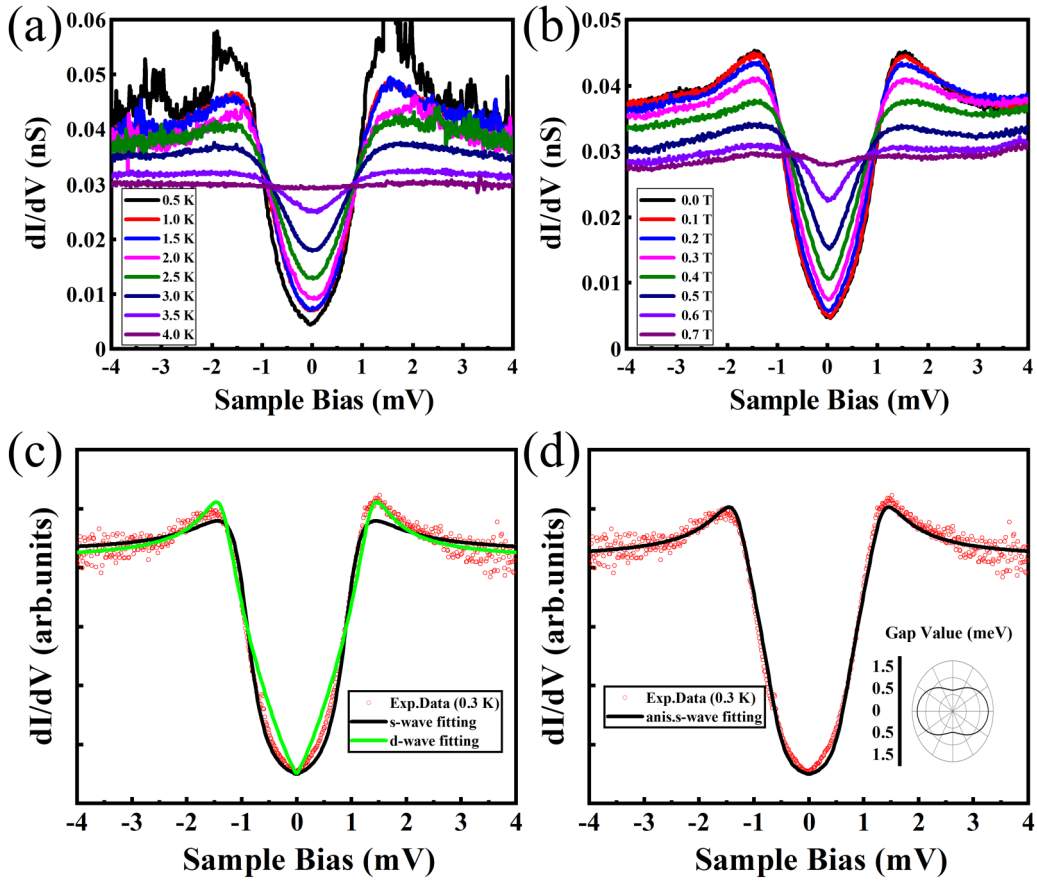

FIG. 2. (a) Scanning tunneling microscopy (STM) differential conductance spectra taken in the temperature range from 0.3 to 4 K ($V_s = -2\,\mathrm{mV}$, $I_t = 800\,\mathrm{pA}$, $V_{\mathrm{rms}} = 100\,\mu\mathrm{V}$, $f = 973\,\mathrm{Hz}$). The curves with different colors show the evolution of the superconducting spectra with increasing temperature. (b) Evolution of the superconducting spectra in magnetic fields up to 0.7 T at 0.3 K ($V_s = -10\,\mathrm{mV}$, $I_t = 500\,\mathrm{pA}$, $V_{\mathrm{rms}} = 100\,\mu\mathrm{V}$, $f = 973\,\mathrm{Hz}$). (c) and (d) Dynes model fitting to the experimental data (c) to single *s* and *d* waves, and (d) anisotropic *s* wave. The red dots are experimental data. The inset to (d) depicts the component used by the Dynes functions to fitting the gap.

two pristine type-II Weyl semimetals $MoTe_2$ (0.1 K) [12] and WTe_2 (below 0.3 K) [20,34].

Our STS results reveal a higher T_c than those reported earlier transport studies [26]. The discrepancy is likely because, in STS, the spectral gap is measured locally on well-ordered regions, while transport measurements are averaged over large areas that can be impacted by scattering and spatial inhomogeneity.

To investigate the superconducting gap symmetry, we used the Dynes function [35] [Eq. (1)] to fit the V-shaped superconducting spectra.

$$\frac{dI}{dV}(V) \propto \Re\left[\frac{V - i\Gamma}{\sqrt{(V - i\Gamma)^2 - \Delta^2}}\right], \tag{1}$$

where Γ is the effective broadening parameter, and Δ is the superconducting gap.

The fits to the superconducting spectra taken at 0.3 K using *s* and *d* waves are shown in Fig. 2(c).

Compared with the experimental data, the conductance at zero bias for the *s* wave shows a flatter bottom. Also, the *s*-wave simulated coherence peaks are broader and display lower differential conductance than the experimental peaks, arguing against simple *s*-wave pairing. As for the *d*-wave fitting, the differential conductance at the Fermi energy is sharper than the *s*-wave fitting, but it is still obviously deviated from the experimental data. Thus, neither *s* nor *d* waves best fit the line shape of the experimental superconducting gap structure.

We also considered anisotropic *s*-wave pairing to fit the superconducting spectra. We chose a twofold symmetric function $\Delta(\vartheta) = \Delta_1 + \Delta_2 \cos 2\vartheta$ to fit the differential conductance, and $\Gamma = 0.25\,\mathrm{meV}$. The best fit, obtained for $\Delta_1 = 0.97\,\mathrm{meV}$ and $\Delta_2 = 0.34\,\mathrm{meV}$, is shown in Fig. 2(d). The temperature and magnetic field dependence of the gap parameter (Δ) and Γ and their Bardeen-Cooper-Schrieffer (BCS) fits are shown in Supplemental Material Fig. S5 [29].

Comparing both the bottom and the shoulder of the experimental differential conductance with the fitted curve, the anisotropic *s*-wave model provides the best fit to the Fermi energy and the coherence peaks, indicating that the superconducting gap of $TaIrTe_4$ is highly anisotropic, with a maximum superconducting gap of 1.31 meV and minimum of 0.63 meV; the gap component is shown in the inset in Fig. 2(d).

With $T_c = 3.9\,\mathrm{K}$ and $\Delta_{\max} = 1.31\,\mathrm{meV}$, the corresponding gap ratio of $2\Delta_{\max}/k_B T_C$ is calculated to be ~7.81, >2 times the value of 3.53 predicted by weak-coupling BCS theory. The value confirms the strong coupling superconductivity in

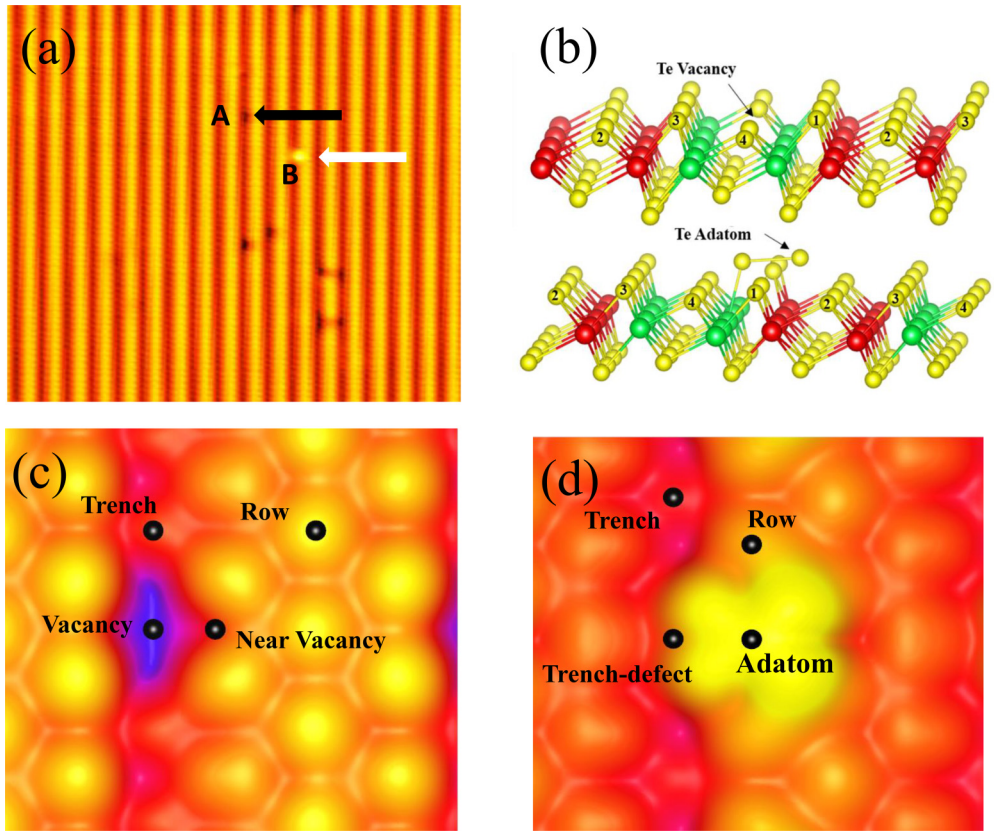

FIG. 3. The defects on $TaIrTe_4$ cleaved (001) surface. (a) Two majority types of atomic defects A and B are observed, denoted by the black and white arrows, respectively (14×14 nm, $V_s = -600$ mV, $I_t = 100$ pA). (b) Ball-and-stick model of $TaIrTe_4$ crystal with the specified atomic sites of the two defects, which are attributed to Te vacancies (Type A) and Te adatoms (Type B). Only the topmost layer is shown, and the numbers label the sites which are consistent with the model in Fig. 1(c). (c) and (d) Simulated scanning tunneling microscopy (STM) images ($V_s = -600$ mV) with representative sites marked for the (c) Te vacancy and (d) Te adatom.

$TaIrTe_4$. Pristine $MoTe_2$ was reported to be weakly superconductive, whereas *S* doping may change it from weak to strong coupling [19,22,36]. From our experiments, $TaIrTe_4$ crystal most likely shows anisotropic *s*-wave superconducting state with strong-coupled pairing <3.9 K.

To interpret the behavior of the superconducting states with applied magnetic field, we measured the superconducting spectra while varying the magnetic field. Figure 2(b) shows a series of superconducting spectra taken at 0.3 K with magnetic field up to 0.7 T, applied along (001) direction of the $TaIrTe_4$ crystal. The coherence peaks slightly shift toward the Fermi energy, gradually becoming broader and eventually disappearing with increase of the magnetic field. The differential conductance at the Fermi energy gradually increases, leading to the disappearance of the superconducting gap for a critical magnetic field of 0.7 T.

Based on Eq. (2) [37], the coherence length of $TaIrTe_4$

$$\xi = \sqrt{\emptyset_0/2\pi H_C}, \tag{2}$$

where $\emptyset_0$ is the flux quantum, H_c is the critical magnetic field, is calculated to be 21.7 nm.

Superconducting states can be enhanced, diminished, or immune to atomic defects, depending on the gap symmetry. Based on Anderson's theorem, in conventional superconductivity, the superconducting gap is immune to nonmagnetic impurities [38]. In unconventional superconductivity, such as the sign-reversal *s*- or *d*-wave superconducting gap, in-gap bound states appear because of nonmagnetic impurity scattering [38–40].

Our Dynes fitting suggests an anisotropic *s*-wave superconducting state in $TaIrTe_4$ (001) surface. In this scenario, coherent Copper pairing states should persist under the perturbation of nonmagnetic impurities. Therefore, the response of the superconducting states to nonmagnetic atomic defects is an indicator of the superconducting pairing symmetry in type-II Weyl semimetal $TaIrTe_4$.

Two structural defects were observed on the $TaIrTe_4$ (001) surface, denoted by A and B in Fig. 3(a). At atomic position A in the trench, the local electronic state is slightly depressed, whereas the local electronic state is significantly enhanced at B (on the "ridges").

DFT calculations of Te vacancies and Te adatoms at various sites were carried out (Supplemental Material Figs. S7 and S8 [29]). Comparisons of experimental and simulated [Figs. 3(c) and 3(d)] STM images led to the identification of Type A defects as vacancy in the trench and Type B as a Te adatom; ball-and-stick models of the optimized structures are given in Fig. 3(b). Structural optimization started from large magnetic moments, but neither of these optimized defect configurations were found to be magnetic. (Certain adatom configurations were magnetic but gave rise to STM images

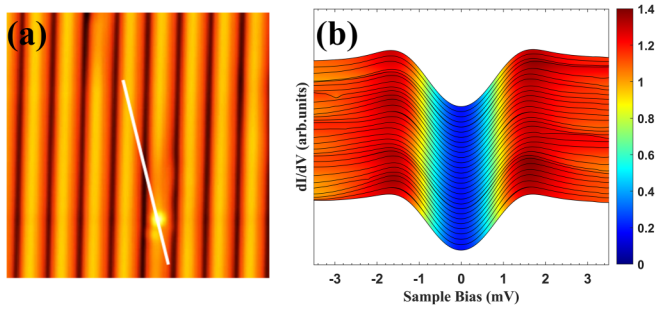

FIG. 4. Spatial distribution of the superconducting spectra. (a) A $TaIrTe_4$ sample with an adatom defect (11×11 nm, $V_s = -50$ mV, $I_t = 100$ pA). (b) Superconducting spectra ($V_s = -2$ mV, $I_t = 800$ pA, $V_{\rm rms} = 100\,\mu$V, $f = 973$ Hz, $T = 1.0$ K) taken along the white line in (a). The spectra taken at the defect site are same with those obtained on the defect free area.

that disagreed strongly with the experimental data.) Therefore, we do not expect the two atomic defects to affect the superconducting states in $TaIrTe_4$, following Anderson's theorem.

The Te vacancy of site 4 Te [using the notation in Fig. 1(c)] causes a slight depression at trenches and is consistent with previously reported structural defects [41]. Adding a Te atom over site 2 resulted in atomic relaxation, including a site 3 Te atom being pushed away, resulting in a complicated bright structure, as shown in Fig. 3(d).

We took differential conductance spectra at the defects, and none of them exhibited obvious resonance states inside or close to the superconducting gap. Figure 4(b) depicts a series of differential conductance spectra with spatial distribution obtained along a white arrow in Fig. 4(a), which crosses an atomic adatom defect. The spatially resolved spectra exhibit uniform line shape, and superconducting spectra obtained at the atomic defect exhibit no obvious in-gap bound states inside the superconducting gap, further indicating the nonmagnetic impurity does not break the Cooper pairing in superconducting states. This observation demonstrates that the nonmagnetic atomic defect on $TaIrTe_4$ (001) surface shows negligible effects on the superconducting state (Supplemental Material Fig. S8 [29]). In *s*-wave superconductors, a resonant peak is induced inside the superconducting gap by magnetic scatters, as experimentally verified by the magnetic scattering on superconductivity in Nb [42]. Therefore, the insensitivity of the superconducting states to nonmagnetic impurities in $TaIrTe_4$ is consistent with the anisotropic *s*-wave pairing symmetry in our Dynes simulation. In addition, the defects show negligible effect on T_c of $TaIrTe_4$ (Supplemental Material Fig. S6 [29]), which is in contrast to the case of the other two type-II Weyl semimetals $MoTe_2$ and WTe_2, where the T_c exhibits significant enhancement by imperfections such as vacancies or impurities [19–22].

In summary, we observed superconducting states in the type-II Weyl semimetal $TaIrTe_4$, with a critical superconducting temperature of 3.9 K and critical magnetic field of 0.7 T. Dynes model simulations indicate an anisotropic *s*-wave superconductivity with strong coupling. Nonmagnetic impurities neither break the superconducting pairing nor induce resonant states inside the superconducting gap, further confirming the *s*-wave pairing gap symmetry. In the future, we plan to investigate the response of the superconducting state to intentionally deposited magnetic impurities to firmly establish such a pairing symmetry in the $TaIrTe_4$ system.

This paper is supported by the National Natural Science Foundation of China (21873014), the Fundamental Research Funds for the Central Universities (Grant No. 2017NT06), the K. C. Wong Education Foundation (GJTD-2018-01), the National Natural Science Foundation of China (U2032204), and by the U.S. Department of Energy, Office of Basic Energy Sciences, Division of Materials Sciences and Engineering under Award No. DE-SC0017632 (computational studies).

[1] A. A. Soluyanov, D. Gresch, Z. Wang, Q. Wu, M. Troyer, X. Dai, and B. A. Bernevig, Nature **527**, 495 (2015).
[2] Y. Sun, S.-C. Wu, M. N. Ali, C. Felser, and B. Yan, Phys. Rev. B **92**, 161107(R) (2015).
[3] K. Deng, G. Wan, P. Deng, K. Zhang, S. Ding, E. Wang, M. Yan, H. Huang, H. Zhang, Z. Xu, J. Denlinger, A. Fedorov, H. Yang, W. Duan, H. Yao, Y. Wu, S. Fan, H. Zhang, X. Chen, and S. Zhou, Nat. Phys. **12**, 1105 (2016).
[4] L. Huang, T. M. McCormick, M. Ochi, Z. Zhao, Michi-To Suzuki, R. Arita, Y. Wu, D. Mou, H. Cao, J. Yan, N. Trivedi, and A. Kaminski, Nat. Mater. **15**, 1155 (2016).
[5] K. Koepernik, D. Kasinathan, D. V. Efremov, S. Khim, S. Borisenko, B. Büchner, and J. van den Brink, Phys. Rev. B **93**, 201101(R) (2016).
[6] Z. Fei, T. Palomaki, S. Wu, W. Zhao, X. Cai, B. Sun, P. Nguyen, J. Finney, X. Xu, and D. H. Cobden, Nat. Phys. **13**, 677 (2017).
[7] Y. Wang, E. Liu, H. Liu, Y. Pan, L. Zhang, J. Zeng, Y. Fu, M. Wang, K. Xu, Z. Huang, Z. Wang, H. Lu, D. Xing, B. Wang, X. Wan, and F. Miao, Nat. Commun. **7**, 13142 (2016).
[8] J. Lai, Y. Liu, J. Ma, X. Zhuo, Y. Peng, W. Lu, Z. Liu, J. Chen, and D. Sun, ACS Nano **12**, 4055 (2018).
[9] G. Sharma, P. Goswami, and S. Tewari, Phys. Rev. B **96**, 045112 (2017).
[10] Z.-M. Yu, Y. Yao, and S. A. Yang, Phys. Rev. Lett. **117**, 077202 (2016).
[11] P. Hosur, X. Dai, Z. Fang, and X.-L. Qi, Phys. Rev. B **90**, 045130 (2014).
[12] Y. Qi *et al.*, Nat. Commun. **7**, 11038 (2016).
[13] Z. Guguchia *et al.*, Nat. Commun. **8**, 1082 (2017).
[14] X. Pan, X. Chen, H. Liu, Y. Feng, Z. Wei, Y. Zhou, Z. Chi, L. Pi, Fei Yen, F. Song, X. Wan, Z. Yang, B. Wang, G. Wang, and Y. Zhang, Nat. Commun. **6**, 7805 (2015).
[15] D. Kang, Y. Zhou, W. Yi, C. Yang, J. Guo, Y. Shi, S. Zhang, Z. Wang, C. Zhang, S. Jiang, A. Li, K. Yang, Q. Wu, G. Zhang, L. Sun, and Z. Zhao, Nat. Commun. **6**, 7804 (2015).
[16] P. Li, J. Cui, J. Zhou, D. Guo, Z. Zhao, J. Yi, J. Fan, Z. Ji, X. Jing, F. Qu, C. Yang, L. Lu, J. Lin, Z. Liu, and G. Liu, Adv. Mater. **31**, 1904641 (2019).

[17] V. Fatemi, S. Wu, Y. Cao, L. Bretheau, Q. D. Gibson, K. Watanabe, T. Taniguchi, R. J. Cava, and P. J. Herrero, Science **362**, 926 (2018).
[18] E. Sajadi, T. Palomaki, Z. Fei, We. Zhao, P. Bement, C. Olsen, S. Luescher, X. Xu, J. A. Folk, and D. H. Cobden, Science **362**, 922 (2018).
[19] F. C. Chen, X. Luo, R. C. Xiao, W. J. Lu, B. Zhang, H. X. Yang, J. Q. Li, Q. L. Pei, D. F. Shao, R. R. Zhang, L. S. Ling, C. Y. Xi, W. H. Song, and Y. P. Sun, Appl. Phys. Lett. **108**, 162601 (2016).
[20] L. Zhu, Q. Li, Y. Lv, S. Li, X. Zhu, Z. Jia, Y. B. Chen, and J. Wen, Nano Lett. **18**, 6585 (2018).
[21] H. Zhang, A. Rousuli, S. Shen, K. Zhang, C. Wang, L. Luo, J. Wang, Y. Wu, Y. Xu, W. Duan, H. Yao, P. Yu, and S. Zhou, Sci. Bull. **65**, 188 (2020).
[22] Y. A. Li, Q. Q. Gu, C. Chen, J. Zhang, Q. Liu, X. Y. Hu, J. Liu, Y. Liu, L. S. Ling, M. L. Tian, Y. Wang, N. Samarth, S. Y. Li, T. Zhang, J. Feng, and J. Wang, Proc. Natl Acad. Sci. **115**, 9503 (2018).
[23] J. W. Luo, Y. N. Li, J. W. Zhang, H. R. Ji, H. Wang, J. Y. Shan, C. X. Zhang, C. Cai, J. Liu, Y. Wang, Y. Zhang, and J. Wang, Phys. Rev. B **102**, 064502 (2020).
[24] E. Haubold, K. Koepernik, D. Efremov, S. Khim, A. Fedorov, Y. Kushnirenko, J. van den Brink, S. Wurmehl, B. Büchner, T. K. Kim, M. Hoesch, K. Sumida, K. Taguchi, T. Yoshikawa, A. Kimura, T. Okuda, and S. V. Borisenko, Phys. Rev. B **95**, 241108(R) (2017).
[25] I. Belopolski, P. Yu, D. S. Sanchez, Y. Ishida, T. Chang, S. S. Zhang, S. Xu, H. Zheng, G. Chang, G. Bian, H. Jeng, T. Kondo, H. Lin, Z. Liu, S. Shin, and M. Z. Hasan, Nat. Commun. **8**, 942 (2017).
[26] Y. Xing, Z. Shao, J. Ge, J. Luo, J. Wang, Z. Zhu, J. Liu, Y. Wang, Z. Zhao, J. Yan, D. Mandrus, B. Yan, X. Liu, M. Pan, and J. Wang, Natl. Sci. Rev. **7**, 579 (2020).
[27] S. Cai, E. Emmanouilidou, J. Guo, X. Li, Y. Li, K. Yang, A. Li, Q. Wu, N. Ni, and L. Sun, Phys. Rev. B **99**, 020503(R) (2019).
[28] Y. Liu, Q. Gu, Y. Peng, S. Qi, N. Zhang, Y. Zhang, X. Ma, R. Zhu, L. Tong, J. Feng, Z. Liu, and J. Chen, Adv. Mater. **30**, 1706402 (2018).
[29] See Supplemental Material at http://link.aps.org/supplemental/10.1103/PhysRevB.103.174508 for additional x-ray diffraction, differential conductance spectra, fitting parameter, and density of states calculations.
[30] W. Zhao, Q. Wang, M. H. Liu, W. H. Zhang, Y. L. Wang, M. Chen, Y. Guo, K. He, X. Chen, Y. Y. Wang, J. Wang, X. C. Xie, Q. Niu, L. L. Wang, X. C. Ma, J. K. Jain, M. H. W. Chan, and Q. K. Xue, Solid State Commun. **165**, 59 (2013).
[31] G. Kresse and J. Furthmüller, Phys. Rev. B **54**, 11169 (1996).
[32] G. Kresse and J. Furthmüller, Comp. Mater. Sci **6**, 15 (1996).
[33] J. P. Perdew, K. Burke, and M. Ernzerhof, Phys. Rev. Lett. **77**, 3865 (1996).
[34] P. L. Cai, J. Hu, L. P. He, J. Pan, X. C. Hong, Z. Zhang, J. Zhang, J. Wei, Z. Q. Mao, and S. Y. Li, Phys. Rev. Lett. **115**, 057202 (2015).
[35] R. C. Dynes, J. P. Garno, G. B. Hertel, and T. P. Orlando, Phys. Rev. Lett. **53**, 2437 (1984).
[36] H. Takahashi, T. Akiba, K. Imura, T. Shiino, K. Deguchi, N. K. Sato, H. Sakai, M. S. Bahramy, and S. Ishiwata, Phys. Rev. B **95**, 100501(R) (2017).
[37] M. Tinkham, *Introduction to Superconductivity* (McGraw-Hill, New York, 1975).
[38] A. V. Balatsky, I. Vekhter, and J.-X. Zhu, Rev. Mod. Phys. **78**, 373 (2006).
[39] S. Mukherjee, M. N. Gastiasoro, and B. M. Andersen, Phys. Rev. B **88**, 134508 (2013).
[40] T. K. Ng and Y. Avishai, Phys. Rev. B **80**, 104504 (2009).
[41] X. Dong, M. Wang, D. Yan, X. Peng, J. Li, W. Xiao, Q. Wang, J. Han, J. Ma, and Y. Shi, ACS Nano **13**, 9571 (2019).
[42] A. Yazdani, B. A. Jones, C. P. Lutz, M. F. Crommie, and D. M. Eigler, Science **275**, 1767 (1997).